Letter

Magnetic separation of rare-earth ions: Transport processes and pattern formation

Zhe Lei,* Barbara Fritzsche, and Kerstin Eckert†

Institute of Fluid Dynamics, Helmholtz-Zentrum Dresden-Rossendorf (HZDR), Bautzner Landstrasse 400, 01328 Dresden, Germany and Institute of Process Engineering and Environmental Technology, Technische Universität Dresden, 01062 Dresden, Germany

(Received 8 July 2020; accepted 28 January 2021; published 11 February 2021)

Despite the relevance of the Kelvin force in many physical and electrochemical systems involving magnetic species, the underlying convective flows are scarcely understood. For that purpose, we simulate a simplified rare-earth system in the presence of competing Kelvin and gravity forces. The results are experimentally validated using interferometry and microscopic particle image velocimetry. Based on the excellent agreement of numerical and experimental results, the underlying mechanism of ions' magnetic separation can be explained, which paves the way for a prospective application in rare-earth beneficiation.

DOI: 10.1103/PhysRevFluids.6.L021901

In a nonuniform magnetic field, the Kelvin force, $\boldsymbol{f}_m$, acts as a body force on a magnetized medium. It can be expressed as the gradient of Gibbs free energy G [1,2],

$$\boldsymbol{f}_m = -\nabla G = \nabla(\mu_0 \boldsymbol{H} \cdot \boldsymbol{M}) \tag{1}$$

where $\boldsymbol{H}$ and $\boldsymbol{M}$ refer to the magnetic field applied and the magnetization of the medium; μ_0 is the vacuum permeability. The applications of the Kelvin force are extremely versatile and include particle separation processes ranging from meter-scale iron scrap down to 100-μm-scale magnetic ore particles [3–5]; or the manipulation of functionalized microparticles [6] in biological systems, extending as far as guided drug delivery in cancer treatment [7]. The Kelvin force supports the adsorption of toxic contaminants in waste water treatment [8], or the structured electrodeposition of metallic alloys [9–12] from paramagnetic ions containing electrolyte. Furthermore, the Kelvin force enables biological material to be magnetically levitated [13]. This elegant procedure allows, e.g., the growth of high-quality protein crystals [14,15] that are needed for a structure-based drug design, thus it is potentially of interest for the viral spike protein.

However, all these techniques require an understanding of the convection driven by the Kelvin force. This understanding is missing and, to a certain extent, more challenging to obtain than for buoyancy-induced convection [16]. This is due to either the superposition with Lorentz-force-driven flows in electrochemical systems [9,12,17] or the opaqueness of the liquid in the case of ferrofluids [1]. Thermomagnetic convection in ferrofluids has therefore mainly been studied indirectly based on heat flux measurements [18–20] or thermosensitive liquid crystal films [21]. The Kelvin force is able to change the critical Rayleigh number for the onset of buoyancy-driven convection in the presence of a homogeneous external magnetic field [18,22]. The flow patterns include stationary magnetoconvection rolls, and vertically or obliquely counterpropagating thermal or thermomagnetic waves [23]. The Soret effect [24] can introduce a nonuniform mass fraction

*z.lei@hzdr.de
†k.eckert@hzdr.de

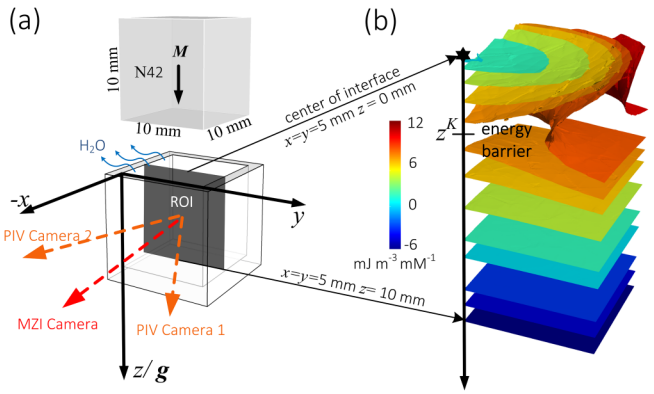

FIG. 1. (a) A rare-earth solution in a cuboid cuvette undergoes evaporation in a nonuniform field of a NdFeB magnet. The laser beams for interferometry and stereo μ-PIV are indicated. (b) Density of the potential energy, Eq. (4), computed with the values given in the text. The position of the energy barrier is marked.

of magnetic nanoparticles into ferrofluids, which generates a gradient in the magnetization. This gradient, which couples with the temperature gradient, might complicate the interpretation of the thermomagnetic convection.

In view of these difficulties, paramagnetic salt solutions are good candidates for studying the features of Kelvin-force-driven convection. Based on a negligible demagnetization field, Eq. (1) can be transformed into [1,2,25]

$$\boldsymbol{f}_m = \frac{\chi_{\mathrm{sol}}}{\mu_0}(\boldsymbol{B}\cdot\nabla)\boldsymbol{B} = \frac{\chi_{\mathrm{sol}}}{2\mu_0}\nabla\boldsymbol{B}^2, \tag{2}$$

where $\boldsymbol{B}$ and χ_{sol} refer to the magnetic flux density and magnetic susceptibility of the solution. Aqueous solutions containing paramagnetic rare-earth (RE) ions are also technologically relevant in solvent extraction, an important process within rare-earth beneficiation [26]. If successful, a magnetic separation step could considerably reduce the amount of less environmentally friendly chemicals needed. Indeed, magnetic separation experiments have shown a robust enrichment of heavy RE species from initially homogeneous solutions [25,27–32]. This was surprising since a change in the ion concentration, $c \propto c_0[1-\exp(-\mu_0 HMV/kT)]$, cannot be expected for Boltzmann-distributed ions as their thermal energy kT is much higher than the magnetic term in G; cf. Eq. (1).

Modeling. By taking dysprosium (Dy) salt, $DyCl_3$, as a representative RE, this puzzle has been solved in [25,29] by actively controlling the evaporation in the setup studied; cf. Fig. 1(a). The separation process is governed by the attractive Kelvin force, Eq. (2), and the opposing gravity force, $\boldsymbol{f}_g = \rho\boldsymbol{g}$ (ρ: density; $\boldsymbol{g}$: gravitational acceleration). The stable base state of the $DyCl_3$ solution before evaporation is characterized by a homogeneous concentration of Dy(III) ions, c_0, leading to both a homogeneous density $\rho_{c_0} = \rho_0(1+\alpha c_0)$ (α: densification factor) and susceptibility, $\chi_{\mathrm{sol}} = \chi_{\mathrm{sol},0} + \chi_{\mathrm{Dy}}c_0$, where ρ_0 and $\chi_{\mathrm{sol},0}$ correspond to pure water. If weak evaporation of the solvent is now admitted, a perturbation, $\Delta c = c - c_0$, appears at the free interface corresponding to an increase of the local Dy(III) concentration, c. This leads to a nonbalanced force increment

$$\Delta\boldsymbol{f} = \Delta\boldsymbol{f}_m + \Delta\boldsymbol{f}_g = \left(\frac{\chi_{\mathrm{Dy}}}{2\mu_0}\nabla\boldsymbol{B}^2 + \rho_0\boldsymbol{g}\alpha\right)\Delta c = -\nabla e_{\mathrm{pot}}\,\Delta c, \tag{3}$$

where $\Delta\boldsymbol{f}_m$ levitates the specific weight, $\Delta\boldsymbol{f}_g$, of the enriched fluid element. The conservative vector field $(\frac{\chi_{\mathrm{Dy}}}{2\mu_0}\nabla\boldsymbol{B}^2 + \rho_0 g\alpha\boldsymbol{e}_z)$ enables derivation of the molar potential energy density field, e_{pot},

introduced in Eq. (3)and given by [25]

$$e_{\mathrm{pot}} = -\left(\frac{\chi_{\mathrm{Dy}}}{2\mu_0}\cdot \boldsymbol{B}^2 + \rho_0 g\alpha\cdot z\right) + \mathrm{const.} \tag{4}$$

Note that the minus sign on the right-hand side of Eq. (4) follows from the definition of the coordinate system in Fig. 1(a). e_{pot} is computed for a quarter of the $DyCl_3$ solution in Fig. 1(b) for the configuration studied [Fig. 1(a)]. The plot shows the existence of an energy barrier at $z = z^K(c_0, \boldsymbol{B})$ which is the local maximum of e_{pot} uniquely defined by its spatial derivative with respect to the z coordinate [25]. It splits the volume of the RE solution into two regions, one dominated by gravity, $z > z^K$, and the other by the Kelvin force, $z < z^K$ [29].

Despite its significance, less is known about the role and pattern formation of a solely Kelvin-force-driven convection, hypothesized in [25]. In this work, we combine the numerical simulation of transport processes in paramagnetic RE solutions with laser techniques to determine velocity and concentration fields. We are able to resolve intriguing features of the Kelvin-force-driven microconvection, facilitating the physical understanding of magnetic RE separation.

The transport process in the rare-earth solution is governed by the incompressible Navier-Stokes equation in Boussinesq approximation,

$$\partial_t \boldsymbol{u} + \boldsymbol{u}\cdot\nabla\boldsymbol{u} = -\frac{1}{\rho_{c_0}}\nabla p' + \nu\nabla^2\boldsymbol{u} - \frac{1}{\rho_{c_0}}\nabla e_{\mathrm{pot}}\Delta c, \tag{5}$$

with $\Delta c = c - c_0$, and the advection-diffusion equation for the Dy(III) concentration, c:

$$\partial_t c + \boldsymbol{u}\cdot\nabla c = \kappa_c\nabla^2 c. \tag{6}$$

The coupling between Eqs. (5) and (6) occurs via the body force terms in Eq. (3) based on the linear correlation of ρ and χ_{sol} with the concentration, c. The reduced pressure p' is $p' = p - \rho_{c_0} g z - e_{\mathrm{pot}} c_0$ where $\rho_{c_0} = \rho_0(1 + \alpha c_0) = 1118$ kg/ m^3 with $\rho_0 = 997$ kg/m^3 water density and $\alpha = 0.243$ M^{-1} [25]. For the molar magnetic susceptibility χ_{Dy}, the kinematic viscosity ν, and the diffusivity κ_c, the following values are adopted: $\chi_{\mathrm{Dy}} = 5.5\times10^{-4}$ M^{-1} [25], $\nu = 1\times10^{-6}$ m^2/s, and $\kappa_c = 1\times10^{-9}$ m^2/s.

Equations (5) and (6) are solved in OpenFOAM inside a $10\times10\times10$ mm^3 cuboid cuvette [Fig. 1(a)] completely filled with an aqueous $DyCl_3$ solution ($c_0 = 0.5$ M). The free-slip interface of the solution, without significant interface deformation [33], is exposed to a fixed evaporation flux, see Supplemental Material [34]. At the time $t = 0$ s, a cuboid N42 NdFeB permanent magnet of 10 mm edge length is placed 2.5 mm above the interface; the magnetization direction is parallel to gravity. The simulations are validated by measuring Δc and $\boldsymbol{u}$ using a Mach-Zehnder interferometer (MZI) [29,35,36] and stereoscopic micro particle image velocimetry (μ-PIV), respectively, in the region of interest (ROI) in Fig. 1(a). See Supplemental Material [34] for experimental and numerical details.

Transport processes. Figures 2(a)–2(d) show snapshots of the continuous transport processes in both the simulation and experiment, marked in Fig. 3. The simulated concentration fields in the y-z plane are spatially averaged along the x axis to compare with the interferometric measurement. The velocity fields simulated are plotted at the position $x = 5$ mm at the focal plane of the μ-PIV system. The kinetic energy of the flow field, $\bar{e}_{\mathrm{kin}} = \rho_0(1 + c_0\alpha)u^2_{\mathrm{mean}}/2c$, based on the mean velocity $u_{\mathrm{mean}} = 1/V\int u(x, y, z)dV$, is shown in Fig. 3.

A comparison between the numerical and the experimental results is presented in Fig. 3(a). To emphasize the very good agreement between experiment and simulation, the experimental $\bar{e}_{\mathrm{kin}}$ curve was shifted by $\boldsymbol{\Delta t_0 = 7}$ s. Both the experiment and the simulation show two maxima in $\bar{e}_{\mathrm{kin}}$, where the onset of the second maximum remarkably happens at almost the same time in experiment and simulation. The motivation for the slight shift of the experimental curve by $\Delta t_0 = 7$ s is the unavoidable difference in the initial conditions between experiment and simulation. When the magnet approaches the solution at $t = 0$ s in the experiment, it takes a time span Δt_0, to cancel out the weak residual convection in the gravity-dominated region which was caused by the

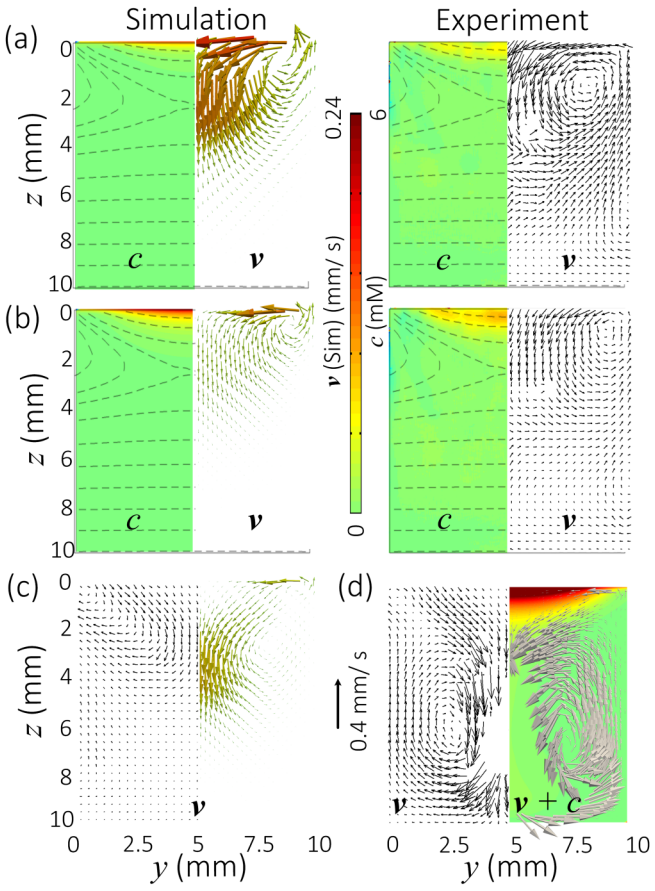

FIG. 2. Comparison of concentration and velocity fields [(a) and (b)] and of velocity fields [(c) and (d)] between experiment (left) and simulation (right) at different times; see Fig. 3(a).

evaporation. The contribution of this residual convection, which does not exist in the simulations, is the reason for slightly faster approaching the first maximum of $\bar{e}_{\mathrm{kin}}$ at a bit elevated values of $\bar{e}_{\mathrm{kin}}$ in the experiments. A further reason for the remaining minor deviations between experiment and simulation with respect to the $\bar{e}_{\mathrm{kin}}$ values of the second maximum lies in the assumption of a constant evaporation flux in the simulation. This flux is the averaged value as measured by the interferometer—see Supplemental Material [34]—while the temporal and spatial distribution of the flux might not be homogeneous in the experiment [37,38].

On analyzing $\bar{e}_{\mathrm{kin}}$ using the numerical results (blue curve) in Fig. 3(a), three distinct phases can be identified. *Phase I* comprises the *onset of the Kelvin-force-driven microconvection* at the interface until a maximum in $\bar{e}_{\mathrm{kin}}$ is achieved. The flow starts immediately when the magnet is placed on the $DyCl_3$ solution [Fig. 1(a)], exposed to a fixed evaporation flux. The reason is that the system becomes unconditionally unstable since the forcing, given by the curl of the total force $\boldsymbol{f}$,

$$\nabla \times \boldsymbol{f} = \nabla \times \boldsymbol{f}_m + \nabla \times \boldsymbol{f}_g = -\nabla c \times \nabla e_{\mathrm{pot}}, \tag{7}$$

is nonzero, as discussed later on. This bears a resemblance to electrodeposition in the presence of Kelvin and Lorentz forces [10,12,39]. The velocity field driven by Eq. (7), see Fig. 2(a), is a toroidal vortex where the flow converges at the center of the interface. The maximum velocity appears at around $t = 8$ s with a peak value reaching around 0.1 mm/s. Figure 3(b) presents a zoom into the

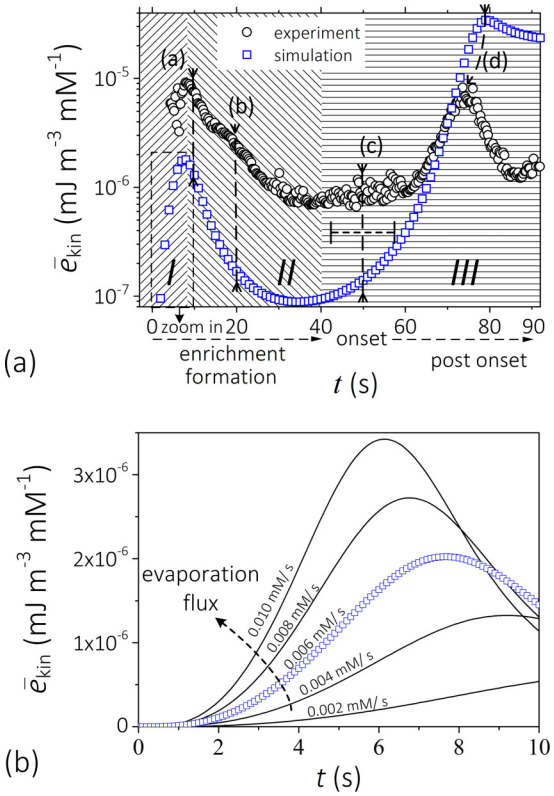

FIG. 3. (a) Mean kinetic energy $\bar{e}_{kin}$ of the flow vs time in the different Phases I–III. The times at which the snapshots were taken in Fig. 2 are indicated by (.). (b) Zoom into Phase I based on simulating the evolution of $\bar{e}_{kin}$ at varying evaporation flux.

initial Phase I by simulating the evolution of $\bar{e}_{kin}$ at different evaporation rates. The mean kinetic energy of the flow increases with the evaporation rate. Likewise, the first maximum is reached earlier.

In *Phase II*, *a priori* nonexpected *attenuation of the Kelvin-force-driven vortex* sets in until a minimum of the kinetic energy is achieved. The attenuation is due to this vortex being squeezed out from the central region towards the walls of the cell; see Figs. 2(a) and 2(b). The underlying mechanism is the entrainment of fresh fluid by the Kelvin vortex. Due to the evaporation, this fluid is enriched there. The toroidal flow pattern of the Kelvin vortex transforms the initial planar, evaporation-driven RE concentration boundary layer (b.l.) into the oval shape also observed in Refs. [25,27–29]. Parallel to the oval deformation, the Dy(III) concentration front propagates deeper into the bulk; cf. Figs. 2(a) and 2(b). The entire enrichment phase, consisting of Phases 1 and 2, is terminated when the propagating c_{Dy} front approaches the position of the energy barrier of the e_{pot}, introduced in Fig. 1(b). The overlapping e_{pot} isocontours in Fig. 2(b) show the barrier position. The region above this energy barrier is the Kelvin-force-dominated region in which the Kelvin force is able to levitate the RE-enrichment layer. It was shown in Ref. [25] that, as the distance between magnet and the interface increases, the Kelvin-force-dominated region narrows down. This shortens the duration of Phase II as Phase III sets in earlier.

Phase III is initiated by an exponential growth in $\bar{e}_{kin}$ due to the *onset of a concentration plume* out of the levitated oval enrichment layer. It is similar to the Rayleigh-Taylor instability emerging from a heavier b.l. overlying lighter fluid, as found, for example, in reactive two-layer

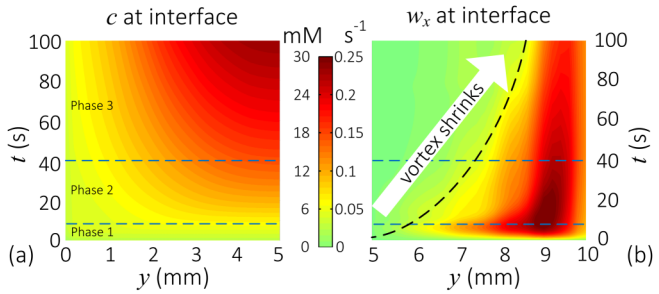

FIG. 4. Space-time plots of line profiles of concentration $c(y)$ (a) and vorticity $\omega_x(y)$ (b) close to interface ($z = 0.5$ mm) from cell rim to cell center.

systems [40]. The onset position, see Fig. 2(c), agrees well with the Kelvin-force-dominated boundary based on the Rayleigh number calculation in Ref. [25] integrating the Kelvin force. Since the minimum of the energy barrier is located at the axis of the magnet (Fig. 1), a single plume emerges instead of multiple plumes [41] as typically found in turbulent Rayleigh-Bénard boundary layers. Due to continuity, the plume-driven flow recirculates along the walls. Thus, a continuous advective mass transfer is maintained between the levitated enrichment in the Kelvin-force-dominated area and the heavier enrichment, advected by the plume at the bottom of cell. Remarkably, however, no mixing occurs between the two regions due to the blocking effect of the energy barrier.

Pattern formation. The space-time plots in Fig. 4 show the simulated line profiles of concentration and vorticity at the interface over the three phases. The concentration profile starts to build up as soon as the magnet is applied at $t = 0$ s; see Fig. 4(a). The enrichment continuously increases at all y positions, the maximum being at the center of the cuvette at $y = 5$ mm. The corresponding vorticity component ω_x, as an indicator for the Kelvin-force-driven microconvection, is plotted in Fig. 4(b). When Phase I begins, the vorticity, ω_x, takes on a nonzero value along nearly the entire interface. Hence, for reasons of symmetry, the Kelvin vortex covers the entire width of the cuvette. With progressing Dy(III) enrichment, the vortex shrinks along the dashed line [Fig. 4(b)]. The center of the Kelvin-force-dominated region thus becomes free of convection, since the Kelvin vortex is squeezed towards the edge of the cuvette. Its vorticity remains constant there as the system continues to evolve.

To discuss the mechanism of this pattern formation, the schema in Figs. 5(a) and 5(b) is used. It shows the changes in the concentration isocontours (solid line) at different times, superimposed by the dashed e_{pot} isocontour. The angle between the normal vectors of the isocontours of c and e_{pot}, ∇c and ∇e_{pot}, is denoted by θ. As shown in Eq. (7), it controls the forcing of the system, given by the curl of the total force, $\nabla \times \boldsymbol{f}$. The evolution of $\nabla \times \boldsymbol{f}$ is depicted in Fig. 5(c).

At the very beginning, a concentration b.l. exists from the evaporation process, which is planar on average and marked by the straight isolines in Fig. 5(a). The angle θ is the maximum. This enables maximum vorticity generation; see Fig. 4(b). Consequently, an enriched fluid element in the b.l., symbolized by the green circle, moves radially inwards towards the center, which coincides with the central axis of the magnet, and turns downwards. As its kinetic energy is too small for it to jump the energy barrier, it recirculates back towards the rim of the cell. The Kelvin-force-driven vortex covers the entire width of the cuvette in Phase I but remains confined between the interface and the energy barrier. This toroidal Kelvin vortex forces the b.l. to be thinner in the near-wall region and thicker in the middle of the cuvette, where the axis of the magnet is placed, as marked by the dashed arrow Fig. 5(a). This process was identified as the mechanism of the oval deformation of the initially planar Dy(III) b.l. in Fig. 2. This deformation feeds back dramatically into the Kelvin-force-driven convection. As the isocontours of c and e_{pot} become more and more parallel in the central part, see Fig. 4(b), θ and hence the forcing $\nabla \times \boldsymbol{f}$ disappear; see Figs. 5(b) and 5(c). As a result, the

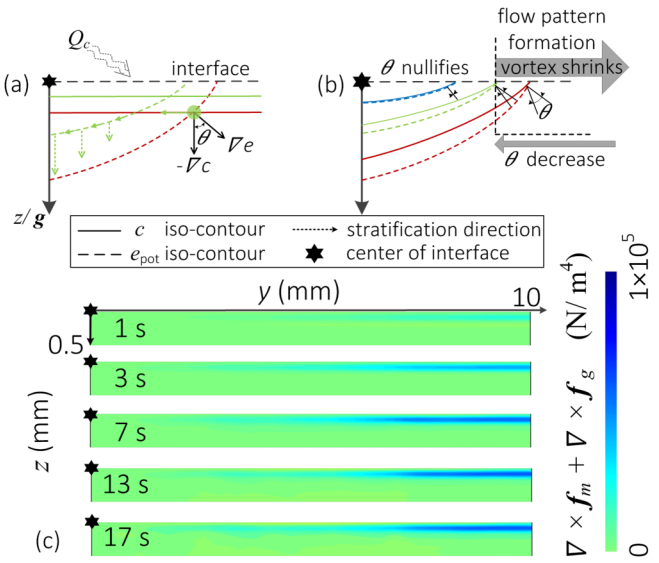

FIG. 5. Schematics explaining the transformation of planar concentration isolines (a) into oval isolines by virtue of the Kelvin-force-driven convection (b) leading to a vanishing angle θ, or forcing, in the Kelvin-force-dominated zone. (c) Snapshots of the $\nabla \times \boldsymbol{f} = -\nabla c \times \nabla e_{\mathrm{pot}}$ at different times.

Kelvin-force-driven vortex vanishes locally and is squeezed towards the rim of the cuvette. Snapshots of $\nabla \times \boldsymbol{f}$ are plotted in Fig. 5(c). The strong rise of $\nabla \times \boldsymbol{f}$ in Phase I is visible. In Phase II, the forcing diminishes but stays on a constant level in the near-wall regions.

The flow pattern inside the gravity-dominated region after the onset of the Rayleigh-Taylor instability in Phase III underlies the same principle as the Kelvin vortex. The release of potential energy by the resulting enrichment plume leads this heavier fluid to settle at the bottom of the cell. The low kinetic energy of the flow compared to the potential energy traps the enriched layer at the bottom. Hence, no significant shift between the isocontours of c and e_{pot} occurs in this gravity-dominated region. Therefore, $\nabla \times \boldsymbol{f} \approx 0$. Thus, active mixing is prevented both between the enriched bottom layer and the bulk, and in the enrichment layer in the Kelvin-force-dominated zone due to the energy barrier.

Summary and conclusions. Based on very good agreement between the numerical simulations and optical measurements, we showed that the magnetic separation of heavy rare-earth ions, such as Dy(III), proceeds in three phases. One precondition is the existence of the trigger process, e.g., evaporation, which establishes an initial concentration inhomogeneity, here a planar Dy(III) ion boundary layer (b.l.) at the free surface. In the presence of a magnetic field, this unconditionally unstable configuration leads to the immediate onset of a Kelvin-force-driven convection in the first phase. The simulations and experiments show that this convection consists of a toroidal vortex extending over the entire width of the cell. This vortex, in connection with evaporation, is responsible for both the further Dy(III) enrichment in the Kelvin-force-dominated zone and the oval deformation of the concentration isolines. The enrichment process is completed at the end of the second phase when the isocontours of c and the potential energy e_{pot} align. This alignment feeds back into the Kelvin-force-driven vortex in an intriguing manner in the second phase: it kills the forcing in the oval region, and squeezes the vortex out of the center towards the wall region. The third phase, a conditionally unstable one, is initiated by the Rayleigh-Taylor instability of the enrichment layer. It sets in when its specific weight can no longer be levitated to its full extent by the Kelvin force. The resulting solutal plume drives a quasisteady recirculation in the gravity-dominated zone of the cell. Active mixing between the gravity- and Kelvin-force-dominated zones is suppressed by

the energy barrier, which is the mechanism which conserves the Dy(III) enrichment layer. With this complexity, the magnetic separation of REs remains a fascinating phenomenon from the viewpoints of both hydrodynamic instability and technological relevance.

We are grateful for financial support by the German Space Agency (DLR) with funds provided by the Federal Ministry of Economics and Technology (BMWi) due to an enactment of the German Bundestag under Grant No. DLR 50WM1741 (project SESIMAG-II). We thank Drs. G. Mutschke, A. Lange, X. Yang, K. Schwarzenberger, S. Heitkam, K. Liu, A. Bashkatov, Y Liao, and F. Schlegel for helpful discussions.

[1] R. E. Rosensweig, *Ferrohydrodynamics* (Dover, Mineola, NY, 2013).
[2] J. M. D. Coey, *Magnetism and Magnetic Materials* (Cambridge University Press, Cambridge, 2010).
[3] J. Oberteuffer, Magnetic separation: A review of principles, devices, and applications, IEEE Trans. Magn. **10**, 223 (1974).
[4] J. Oberteuffer, High gradient magnetic separation, IEEE Trans. Magn. **9**, 303 (1973).
[5] C. Hoffmann, M. Franzreb, and W. H. Holl, A novel high-gradient magnetic separator (HGMS) design for biotech applications, IEEE Trans. Appl. Supercond. **12**, 963 (2002).
[6] N. Pamme and C. Wilhelm, Continuous sorting of magnetic cells via on-chip free-flow magnetophoresis, Lab Chip **6**, 974 (2006).
[7] R. Jurgons, C. Seliger, A. Hilpert, L. Trahms, S. Odenbach, and C. Alexiou, Drug loaded magnetic nanoparticles for cancer therapy, J. Phys.: Condens. Matter **18**, S2893 (2006).
[8] A. Misra, C. Zambrzycki, G. Kloker, A. Kotyrba, M. H. Anjass, I. Franco Castillo, S. G. Mitchell, R. Güttel, and C. Streb, Water purification and microplastics removal using magnetic polyoxometalate-supported ionic liquid phases (magpom-silps), Angew. Chem., Int. Ed. **59**, 1601 (2020).
[9] K. Tschulik, C. Cierpka, A. Gebert, L. Schultz, C. J. Kaehler, and M. Uhlemann, In situ analysis of three dimensional electrolyte convection evolving during the electrodeposition of copper in magnetic gradient fields, Anal. Chem. **83**, 3275 (2011).
[10] P. Dunne, L. Mazza, and J. M. D. Coey, Magnetic Structuring of Electrodeposits, Phys. Rev. Lett. **107**, 024501 (2011).
[11] M. Uhlemann, K. Tschulik, A. Gebert, G. Mutschke, J. Fröhlich, A. Bund, X. Yang, and K. Eckert, Structured electrodeposition in magnetic gradient fields, Eur. Phys. J.: Spec. Top. **220**, 287 (2013).
[12] G. Mutschke, K. Tschulik, T. Weier, M. Uhlemann, A. Bund, and J. Fröhlich, On the action of magnetic gradient forces in micro-structured copper deposition, Electrochim. Acta **55**, 9060 (2010).
[13] A. K. Geim, Nobel lecture: Random walk to graphene, Rev. Mod. Phys. **83**, 851 (2011).
[14] M. C. R. Heijna, P. W. G. Poodt, K. Tsukamoto, W. J. De Grip, P. C. M. Christianen, J. C. Maan, J. L. A. Hendrix, W. J. P. Van Enckevort, and E. Vlieg, Magnetically controlled gravity for protein crystal growth, Appl. Phys. Lett. **90**, 264105 (2007).
[15] J. R. Helliwell and N. E. Chayen, A down-to-earth approach, Nature (London) **448**, 658 (2007).
[16] J. S. Turner, *Buoyancy Effects in Fluids* (Cambridge University Press, Cambridge, 1979).
[17] K. Tschulik, C. Cierpka, G. Mutschke, A. Gebert, L. Schultz, and M. Uhlemann, Clarifying the mechanism of reverse structuring during electrodeposition in magnetic gradient fields, Anal. Chem. **84**, 2328 (2012).
[18] L. Schwab, U. Hildebrandt, and K. Stierstadt, Magnetic bénard convection, J. Magn. Magn. Mater. **39**, 113 (1983).
[19] H. Engler and S. Odenbach, Parametric modulation of thermomagnetic convection in magnetic fluids, J. Phys.: Condens. Matter **20**, 204135 (2008).
[20] M. Lajvardi, J. Moghimi-Rad, I. Hadi, A. Gavili, T. D. Isfahani, F. Zabihi, and J. Sabbaghzadeh, Experimental investigation for enhanced ferrofluid heat transfer under magnetic field effect, J. Magn. Magn. Mater. **322**, 3508 (2010).

[21] S. A. Suslov, A. A. Bozhko, A. S. Sidorov, and G. F. Putin, Thermomagnetic convective flows in a vertical layer of ferrocolloid: Perturbation energy analysis and experimental study, Phys. Rev. E **86**, 016301 (2012).
[22] A. N. Afifah, S. Syahrullail, and N. A. C. Sidik, Magnetoviscous effect and thermomagnetic convection of magnetic fluid: A review, Renewable Sustainable Energy Rev. **55**, 1030 (2016).
[23] S. A. Suslov, Thermomagnetic convection in a vertical layer of ferromagnetic fluid, Phys. Fluids **20**, 084101 (2008).
[24] L. Sprenger, A. Lange, A. Y. Zubarev, and S. Odenbach, Experimental, numerical, and theoretical investigation on the concentration-dependent Soret effect in magnetic fluids, Phys. Fluids **27**, 022001 (2015).
[25] Z. Lei, B. Fritzsche, and K. Eckert, Stability criterion for the magnetic separation of rare-earth ions, Phys. Rev. E **101**, 013109 (2020).
[26] F. Xie, T. A. Zhang, D. Dreisinger, and F. Doyle, A critical review on solvent extraction of rare earths from aqueous solutions, Miner. Eng. **56**, 10 (2014).
[27] X. Yang, K. Tschulik, M. Uhlemann, S. Odenbach, and K. Eckert, Enrichment of paramagnetic ions from homogeneous solutions in inhomogeneous magnetic fields, J. Phys. Chem. Lett. **3**, 3559 (2012).
[28] B. Pulko, X. Yang, Z. Lei, S. Odenbach, and K. Eckert, Magnetic separation of Dy (III) ions from homogeneous aqueous solutions, Appl. Phys. Lett. **105**, 232407 (2014).
[29] Z. Lei, B. Fritzsche, and K. Eckert, Evaporation-assisted magnetic separation of rare-earth ions in aqueous solutions, J. Phys. Chem. C **121**, 24576 (2017).
[30] K. Kołczyk, M. Wojnicki, D. Kutyła, R. Kowalik, P. Żabiński, and A. Cristofolini, Separation of HO^{3+} in static magnetic field, Arch. Metall. Mater **61**, 1919 (2016).
[31] I. R. Rodrigues, L. Lukina, S. Dehaeck, P. Colinet, K. Binnemans, and J. Fransaer, Magnetomigration of rare-earth ions triggered by concentration gradients, J. Phys. Chem. Lett. **8**, 5301 (2017).
[32] K. Kolczyk-Siedlecka, M. Wojnicki, X. Yang, G. Mutschke, and P. Zabinski, Experiments on the magnetic enrichment of rare-earth metal ions in aqueous solutions in a microflow device, J. Flow Chem. **9**, 175 (2019).
[33] B. Fritzsche, G. Mutschke, T. J. Meinel, X. Yang, Z. Lei, and K. Eckert, Oscillatory surface deformation of paramagnetic rare-earth solutions driven by an inhomogeneous magnetic field, Phys. Rev. E **101**, 062601 (2020).
[34] See Supplemental Material at http://link.aps.org/supplemental/10.1103/PhysRevFluids.6.L021901 for details of the theoretical model and its numerical solution.
[35] Z. Lei, Ch. Haberstroh, S. Odenbach, and K. Eckert, Heat transfer enhancement in magnetic cooling by means of magnetohydrodynamic convection, Int. J. Refrig. **62**, 166 (2016).
[36] Z. Lei, X. Yang, Ch. Haberstroh, B. Pulko, S. Odenbach, and K. Eckert, Space- and time-resolved interferometric measurements of the thermal boundary layer at a periodically magnetized gadolinium plate, Int. J. Refrig. **56**, 246 (2015).
[37] H. Mancini and D. Maza, Pattern formation without heating in an evaporative convection experiment, Europhys. Lett. **66**, 812 (2004).
[38] F. Doumenc, T. Boeck, B. Guerrier, and M. Rossi, Transient Rayleigh–Bénard–Marangoni convection due to evaporation: a linear non-normal stability analysis, J. Fluid Mech. **648**, 521 (2010).
[39] G. Mutschke, K. Tschulik, M. Uhlemann, A. Bund, and J. Fröhlich, Comment on Magnetic Structuring of Electrodeposits, Phys. Rev. Lett. **109**, 229401 (2012).
[40] A. De Wit, Chemo-hydrodynamic patterns and instabilities, Annu. Rev. Fluid Mech. **52**, 531 (2020).
[41] A. Vreme, F. Nadal, B. Pouligny, P. Jeandet, G. Liger-Belair, and P. Meunier, Gravitational instability due to the dissolution of carbon dioxide in a Hele-Shaw cell, Phys. Rev. Fluids **1**, 064301 (2016).